

Research Paper

Constraining Europa's ice shell thickness with fundamental mode surface wave dispersion



Ross R. Maguire ^{a,b,*}, Nicholas C. Schmerr ^b, Vedran Lekić ^b, Terry A. Hurford ^c, Lenore Dai ^d, Alyssa R. Rhoden ^e

^a Department of Earth and Planetary Sciences, University of New Mexico, Albuquerque, NM, United States of America

^b Department of Geology, University of Maryland, College Park, MD, United States of America

^c Planetary Geology, Geophysics and Geochemistry Laboratory, NASA Goddard Spaceflight Center, Greenbelt, MD, United States of America

^d School for Engineering of Matter, Transport and Energy, Arizona State University, Tempe, AZ, United States of America

^e Southwest Research Institute, Boulder, CO, United States of America

ARTICLE INFO

ABSTRACT

Keywords:

Europa
Ice shell thickness
Seismology
Icy ocean worlds
Subsurface ocean

Determining the thickness of Europa's outer ice shell is a key factor for understanding Europa's internal dynamics, evolution, and potential habitability. As such, one of the primary goals of any future lander mission to Europa would be to constrain the thickness of the ice shell and confirm the presence of a global subsurface ocean. Tidally induced ice fracturing events provide a natural source of seismic energy to illuminate the subsurface, thus a seismic instrument onboard a future lander mission could provide a promising means to probe ice shell thickness. A variety of seismic techniques could be used to constrain Europa's interior structure and dynamics, including body wave, surface wave, and normal mode seismology. Here, we use numerical simulations of seismic wave propagation on Europa in order to investigate the potential of using long period dispersion measurements of Rayleigh and flexural waves to constrain the ice shell thickness. Since the sensitivity kernels of group velocity dispersion measurements depend strongly on the structure of the ice shell, inverting for ice shell thickness is a non-linear problem.

To address this, we use either a grid search or Markov chain Monte Carlo inversion approach, and test the method on a variety of plausible models of Europa's interior. Additionally, we demonstrate our approach in a "blind" inversion using the 1 week long synthetic catalogs of Europa's seismicity from Panning et al. (2018). We find that under most scenarios, group velocity dispersion measurements between periods of 25–250 s can constrain Europa's ice shell thickness to within several km uncertainty, although the method becomes increasingly inaccurate for thicker ice shells and at large epicentral distances. Our results, which suggest that surface waves from naturally occurring ice fracturing events on Europa can be used to help determine ice shell thickness, may help set instrument requirements for spaceflight capable seismometers aimed at exploring icy ocean worlds.

1. Introduction

Geophysical evidence and spacecraft imagery from the Galileo mission suggests that Europa's ice shell is underlain by a global water ocean (Carr et al., 1998; Greenberg et al., 1998; Kivelson et al., 2000), however, the thickness of the ice shell is uncertain. Current estimates of the ice shell thickness span a wide range, from just a few kilometers to tens of kilometers (Carr et al., 1998; Nimmo et al., 2003; Quick and Marsh, 2015), and the possibility remains that the entire water shell is frozen (e.g., Pappalardo et al., 1999). Constraining the ice shell

thickness is a key goal of future missions to Europa since it provides important controls on the dynamics of the ice-ocean system and has implications for Europa's potential to harbor life. The upcoming NASA Europa Clipper mission, set to launch in 2024, will carry the Radar for Europa Assessment and Sounding: Ocean to Near-surface (REASON) ice-penetrating radar instrument, which has the potential to provide the first direct measurements of Europa's ice shell thickness, as well as to constrain the presence of pockets of liquid water within the shell (e.g., Lam et al., 2018). However, ice shell thickness determinations from radar measurements may be limited in the case of a thick or highly

* Corresponding author at: University of New Mexico, Albuquerque, NM, United States of America.
E-mail address: rmaguire@unm.edu (R.R. Maguire).

scattering ice shell structure (e.g., Eluszkiewicz, 2004). Thus, other potential geophysical methods for measuring ice shell thickness should be explored. One promising method is to place a seismic instrument on Europa's surface, which could take advantage of naturally occurring seismic events to probe ice shell structure and thickness, as well as to characterize the tectonic environment. A drawback to this method is that it would require a costly lander mission which may only be operable for several weeks or less due to the harsh radiation environment caused by Jupiter's magnetic field. Nonetheless, seismology would likely provide the best means for accurately constraining Europa's structure and understanding its interior dynamics.

Several previous studies have explored how seismology might be used to determine the thickness of Europa's ice shell using a variety of techniques. Kovach and Chyba (2001) first suggested using the frequency dependence of seismic surface waves (i.e., surface wave dispersion) as a diagnostic feature of ice shell thickness. Additionally, they proposed the existence of vertically polarized shear waves known as Crary waves in Europa's ice shell. These waves, which are observed in floating sea ice on Earth (Crary, 1954), have a roughly monochromatic frequency content which is diagnostic of ice thickness. If Crary waves are clearly observed on Europa they would verify the presence of a subsurface ocean, and their frequency content would uniquely constrain the thickness of the ice shell. Lee et al. (2003) modeled high frequency (> 1 Hz) synthetic seismograms from ice cracking events on Europa in order to explore how a single 3-component seismometer could constrain ice shell thickness from the travel times of ice-bottom reflections (i.e., echo sounding). They concluded that ice fracturing events with sufficient energy to generate observable ice bottom reflections are likely to be frequent enough to occur within the short time frame of a Europa lander mission. Panning et al. (2006) computed waveforms using normal mode summation to explore how long period seismology (> 10 s) could constrain ice shell thickness. They found that long period vertically polarized flexural waves could be the highest amplitude signals on seismic records and verified that fundamental mode group velocity dispersion curves of P-SV polarized surface waves (Rayleigh or flexural waves) are a useful diagnostic of ice shell thickness. Additionally, they suggested that the peak displacements from ice faulting events in Europa's outer shell could be large enough to be measured using orbital laser range-finding approaches with mm accuracy, thus diminishing the need for a ground-based instrument to measure group velocity dispersion. However, events that generate flexural waves with large enough amplitude to be observed from orbit are likely to be rare. Stähler et al. (2018) used synthetic waveform modeling to perform an in-depth exploration of the broadband seismic wavefield in icy ocean worlds, including Europa. They outline a method to constrain ice shell thickness by using the travel times of multiple reflections contained in the coda of body waves from distant events. This method is advantageous since it depends only on the travel time delay between multiples and hence does not require a determination of event distance. However, challenges may arise if wave scattering is strong enough to obscure the multiples.

In this paper, our goal is to explore the practicality of using long period surface wave dispersion measurements from a single ground based seismic instrument in order to invert for ice shell thickness. The benefit of using long period seismology is that low frequency surface waves such as flexural waves are expected to be among the largest signals of ground motion on icy ocean worlds, and they are not significantly affected by shallow scattering and attenuation. Additionally, the frequency range used to constrain ice shell structure is likely to be separated from shorter period environmental or lander noise. In our approach, we forward model synthetic waveforms propagating through Europa's interior in order to characterize the predicted patterns of surface wave dispersion. We treat our synthetic seismograms as inputs for an inversion to recover ice shell structure, while incorporating some of the practical limitations of single station seismology on Europa. The results show that seismology provides an independent means of determining ice shell thickness that is complementary to satellite-based ice

penetrating radar such as will be on board the forthcoming Europa Clipper mission. We argue that in order to maximize the scientific return on investment of any future Europa lander mission, an onboard seismic instrument should be capable of measuring ground displacement at periods of up to 250 s or longer.

2. Forward modeling

2.1. Radial models of Europa's interior

Our computational seismic experiments rely on plausible models of the seismic velocity, density, and attenuation structure (Q^{-1}) of Europa's interior. In this study, we use the physically self-consistent structural models of Cammarano et al. (2006), which satisfy mass and moment of inertia constraints. The structural models (Fig. 1) depend on the assumed composition and thermal profiles in the core, mantle, and water-ice shell. Cammarano et al. (2006) assumed a pure-water shell, a pyrolytic mantle, and a core composed of either pure Fe or a 80% Fe 20% S mixture. While they considered both hot and cold end-member mantle thermal profiles, the ice shell structure is largely insensitive to the choice of thermal profile for a fixed ice shell thickness. Here, we use the set of 1D radial profiles calculated using the hot end-member scenario, which includes ice shell thicknesses of 5, 10, 20, and 40 km (Fig. 1). In each of the models, the boundary between the water/ice and silicate mantle is 127 km deep, and the core-mantle boundary is 1098 km deep. The seismic velocity structure within the ice shell is close to constant, with $V_P = 4$ km/s and $V_S = 2$ km/s, although both V_P and V_S increase slightly in the upper several km where the ice is in a cold conductive regime. The shear quality factor $Q\mu$ decreases from greater than 1000 in the cold conductive portion of the ice shell, to less than 10 in the warmer convective portion of the ice shell. The bulk quality factor Q_k is assumed to be large enough to be ignored. Our models are in general agreement with recent structural models by Vance et al. (2018a), particularly for the velocity of the ice shell, which is our primary focus in this work.

2.2. Sources of seismicity on Europa

Tidal interaction between Jupiter and Europa creates stress within Europa's interior, some of which is dissipated as seismic energy (e.g., Vance et al., 2018b; Hurford et al., 2019). Satellite imagery and surface topography shows evidence for multiple styles of faulting in the ice shell, including diurnal tensile cracking (i.e., opening and closing of fractures) (Greenberg et al., 1998; Lee et al., 2003), strike slip faulting (Hoppa et al., 1999), and normal faulting (Nimmo and Schenk, 2006). Tidally driven seismicity may also occur within Europa's silicate mantle, although the seismic signals would likely be difficult to observe at the surface due to the decoupling effect of the global ocean layer (e.g., Panning et al., 2006). While it is reasonable to expect that there is ongoing ice-tectonics on Europa that would produce seismic events during the timeframe of a lander mission, their frequency of occurrence and source characteristics remain highly uncertain. Europa may also host additional sources of seismicity due to impacts (Tsuiji and Teanby, 2016), cryovolcanism, and long period surface motion caused by circulation in the subsurface ocean Vance et al. (2018b).

Panning et al. (2018) modeled Europa's seismicity by assuming that tidally forced ice-cracking events follow a Gutenberg-Richter relationship. Under this assumption, the magnitude frequency distribution of seismic events can be determined if the cumulative annual seismic moment ΣM_o , the maximum event size M_o^* , and the b -value (i.e., slope of the Gutenberg-Richter relationship) are known (e.g., Golombek et al., 1992). While none of these parameters are strongly constrained in the case of Europa, expectations can be guided by considering seismicity in both the Earth and the Moon. Seismicity in the Earth's crust is typically observed to have a b -value of 1, although it varies slightly with tectonic setting (e.g., Giulia and Wiemer, 2010). The b -value of seismicity in Earth's cryosphere varies widely depending on region and style of

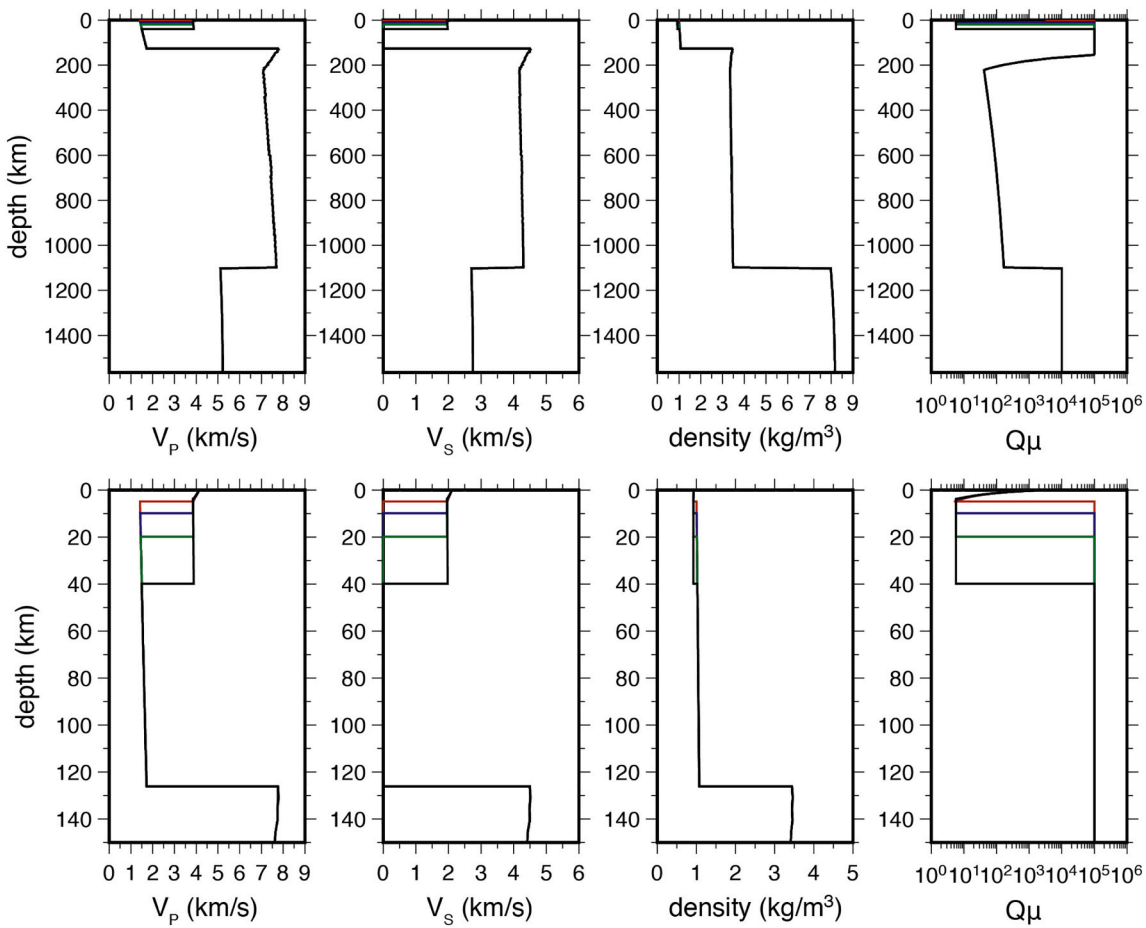


Fig. 1. Top row, from left to right: V_p , V_s , ρ , and $Q\mu$ of 1D Europa structure models. Bottom row: Same as top row but zoomed-in on the water/ice shell structure. The red, blue, green, and black lines show structural models with 5, 10, 20, and 40 km thick ice shells, respectively.

seismic events. For example, Bassis et al. (2007) found a b -value of 1 ± 0.2 for seismicity related to rift propagation in the Amery Ice Shelf in Antarctica, which may be a roughly analogous setting to tensile fracturing within Europa's ice shell. On the other hand, Helmstetter et al. (2015) found a b -value of 3.5 for icequakes occurring deep in the Glacier d'Argentière alpine glacier. The reported b -values of lunar seismicity recorded by the Apollo seismic network range from 0.5 (Nakamura, 1977) to 1.78 (Lammlein et al., 1974) depending on the catalog that is considered. In a re-analysis of the catalog of 28 known shallow moonquakes, Hurford et al., 2019 noted that the b -value is likely biased due to catalog incompleteness for magnitudes below M_w 2.9. When fitting the catalog of events above this threshold they find a b -value of close to 1.

If lunar seismicity is predominantly driven by tides, the Apollo seismic data may provide insight into the expected tidally driven cumulative moment release of Europa. While deep moonquake activity is clearly related to tidal periodicity (e.g., Lammlein, 1977), the origin of shallow moonquakes, which account for the majority of the lunar seismic moment release, is debated. Oberst (1987) found that shallow moonquakes are associated with high stress drops (typically larger than 1 MPa), which exceeds the expected tidal stresses in the Moon of approximately 0.1 MPa (Cheng and Toksöz, 1978), which may suggest a non-tidal origin. However, Hurford et al., 2019 argue that shallow moonquakes could be releasing stress that has built up on faults over multiple tidal cycles. Additionally, Shirley (1986) found a correlation between position of the Earth-Moon system and the timing of shallow moonquakes, suggesting that shallow moonquakes could be tidally triggered. The cumulative moment release of the shallow moon quakes is roughly 10^{15} Nm (e.g., Oberst, 1987), which may serve as a reasonable estimate of ΣM_o for the Moon. Given the large tidal forces experienced by

Europa, it is likely that ΣM_o is much larger on Europa than the Moon (e.g., Vance et al., 2018b), although estimates are complicated by the fact that tidal energy can be aseismically dissipated in the warm ductile portion of Europa's ice shell. While estimating M_o^* for Europa is difficult given the lack of seismic data, some constraints can be placed by analyzing previous faulting events based from surface morphology. For example, Nimmo and Schenk (2006) identified two normal faults on Europa's surface and suggested that the larger of the two could host a M_w 5.3 event (seismic moment, $M_0 = 1.1 \times 10^{17}$ Nm) assuming a shear modulus in the shallow subsurface of 0.4 GPa.

In their models of Europan seismicity, Panning et al. (2018) assumed a b -value of 1, and considered a range of values for ΣM_o and M_o^* . From these models they constructed 7-day synthetic records of ground motion, built from catalogs of randomly located events that satisfy the Gutenberg-Richter statistics. Their preferred model, which assumes a cumulative moment release of $\Sigma M_o = 10^{17}$ Nm and a maximum event magnitude of $M_o^* = 10^{18.5}$ Nm, predicts that Europa hosts around 1 M_w 3 event per week. Interestingly, their modeling predicts that Europa's background noise, which consists of the superposition of abundant micro-seismic ice cracking events, is very quiet (-180 dB or lower for their preferred model). While this would be beneficial for recording seismic events, it would inhibit methods that utilize ambient noise for structural imaging (e.g., Compaire et al., 2021; Sens-Schönenfelder and Larose, 2010) if the noise level is below the sensitivity of the seismic instrument. Recently, Hurford et al., 2019 estimated the seismicity of Europa based on a scaling between tidal dissipation and seismicity in the Earth-Moon system, and found that over a 10-orbit cycle (35.5 Earth days), Europa could host several M_w 5 events, and as many as 100 or more M_w 3 events. Over this time period, Europa's cumulative seismic

moment release would be $\Sigma M_o = 1.5 \times 10^{17}$ Nm. Additionally, their model predicts that seismicity is both spatially and temporally variable, with the highest seismicity occurring near the poles during times of high tidal dissipation, which could guide efforts at determining an optimal landing site for a future mission.

In the modeling that follows, we use a Mw 3 source as our representative example since it is plausible that a seismic lander mission would record at least one event of this magnitude during the course of the mission. Additionally, a Mw 3 event would likely produce seismic waves that are observable on a regional to global scale. For simplicity, we ignore source radiation pattern complexity, and assume that sources radiate energy that is recorded on vertical, radial, and transverse component seismograms.

2.3. Seismic wavefield simulations

To simulate seismic wave propagation through Europa's interior, we use the spectral element method (SEM) based code AxiSEM (Nissen-Meyer et al., 2014), combined with Instaseis (Van Driel et al., 2015), which allows efficient storage and retrieval of synthetic Green's functions for arbitrary sources and receiver locations. We create synthetic databases accurate to periods as low as 5 s for the radially symmetric structural models of Europa's interior shown in Fig. 1. In this paper, our focus is on long period surface waves traveling within the ice shell. For a more complete discussion of the seismic wavefield on Europa and other ice covered ocean-bearing satellites see Stähler et al. (2018).

Fig. 2 shows an example of a 1-h long 3-component record section calculated in a 10 km thick ice shell model. The synthetics were computed for slip on a normal fault placed at the surface. The source time function is a Gaussian pulse with a width equal to the minimum resolved mesh period of 5 s. The vertical (Z) component record section is dominated by surface wave energy that arrives as a train of short period Rayleigh waves followed by long period flexural waves, in which the entire ice shell moves up and down. These waves exhibit a characteristic dispersion, with shorter period energy arriving first since long period energy is more sensitive to the low velocity subsurface ocean layer. As shown by Panning et al. (2006), flexural wave amplitudes are larger in the case of thinner ice shells. They would not exist if Europa's entire water shell were frozen, thus simply detecting flexural waves would confirm the presence of a subsurface ocean. Due to their elliptical motion, Rayleigh waves are also present on the radial (R) component, while the flexural waves are less apparent. An additional long period surface wave named the Longitudinal wave (LL) is strongly apparent on the R component, but only weakly present on the Z component. On the transverse (T) component, the long period Toroidal wave (LQ), which travels at the velocity of Vs in the ice shell (e.g., Stähler et al., 2018), is the only phase visible at most distances.

The characteristics of each of these waves is affected by the assumed

attenuation structure, which has a large uncertainty in the case of Europa. In Fig. 3, we show an example of Z, R, and T component displacement synthetics for a 10 km thick ice shell with different assumptions about attenuation. The synthetics are calculated for a Mw 3 normal faulting source at an epicentral distance of 20 degrees (546 km). We consider two end-member cases for attenuation. The first, shown in orange, is the highly attenuating (low Q) endmember, which is taken as the hot geotherm scenario from Cammarano et al. (2006). For the low attenuation endmember, shown in blue, we neglect attenuation entirely. While physically implausible, this model allows us to explore the range of possible behaviors without making subjective choices about the upper limit of Q in the ice shell. In both cases, the predominant long period surface wave phases, including the flexural wave, the Longitudinal wave, and the Toroidal wave are present, although some important differences are evident. Most obviously, attenuation diminishes peak amplitudes and introduces a phase delay even at long periods. In the case where attenuation is neglected, two additional seismic phases are apparent. First, on the R component, the monochromatic Crary wave arrives shortly after the Longitudinal wave. As noted in Section 1, observations of this wave are significant since its characteristic frequency is diagnostic of ice shell thickness. Its absence in the high attenuation model suggests it may be difficult to record in real data, even at regional distances. When attenuation is neglected, the transverse component displays a clear high frequency Love wave train following the arrival of the Toroidal wave. In the low-Q endmember scenario this phase vanishes.

2.4. Surface wave dispersion

Surface waves polarized with P-SV motion (Rayleigh and flexural waves) travel in different regimes depending on the ratio between wavelength and ice shell thickness. When wavelengths are shorter than the thickness of the ice, the waves travel with both a group velocity and phase velocity of about 0.91Vs (i.e., they are non-dispersive). At long period, when wavelength exceeds the ice shell thickness, the waves are sensitive to the underlying ocean and exhibit dispersive behavior, with group velocity proportional to the square root of frequency. We note that while flexural waves exhibit a characteristic dispersion, the distinction between Rayleigh and flexural waves is a consequence of the boundary conditions. Since short period surface waves are not sensitive to the base of the ice shell, the Rayleigh wave regime is analogous to wave propagation in an elastic halfspace, while the flexural wave regime is analogous to plate bending caused by the confinement of long period waves trapped in the ice shell. As discussed by Panning et al. (2006), the frequency dependence of travel times of these waves is diagnostic of ice shell thickness. In Fig. 4, we show several examples of how this characteristic dispersion is measured from the synthetics by performing group velocity analysis using the multiple filter technique (Dziewonski

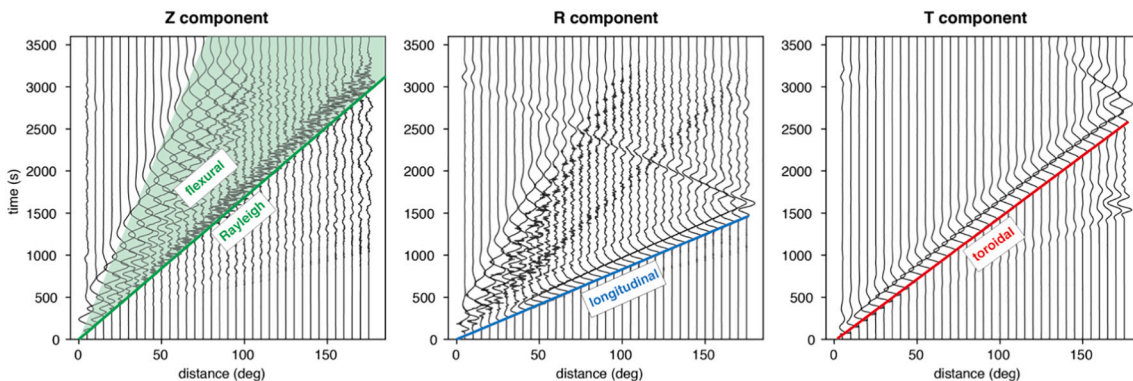


Fig. 2. Displacement synthetics for 10 km thick ice shell, calculated for a Mw3 normal-faulting event placed at the surface. Major surface wave phases traveling in the ice shell are labeled. Waveforms are filtered between 5 and 250 s.

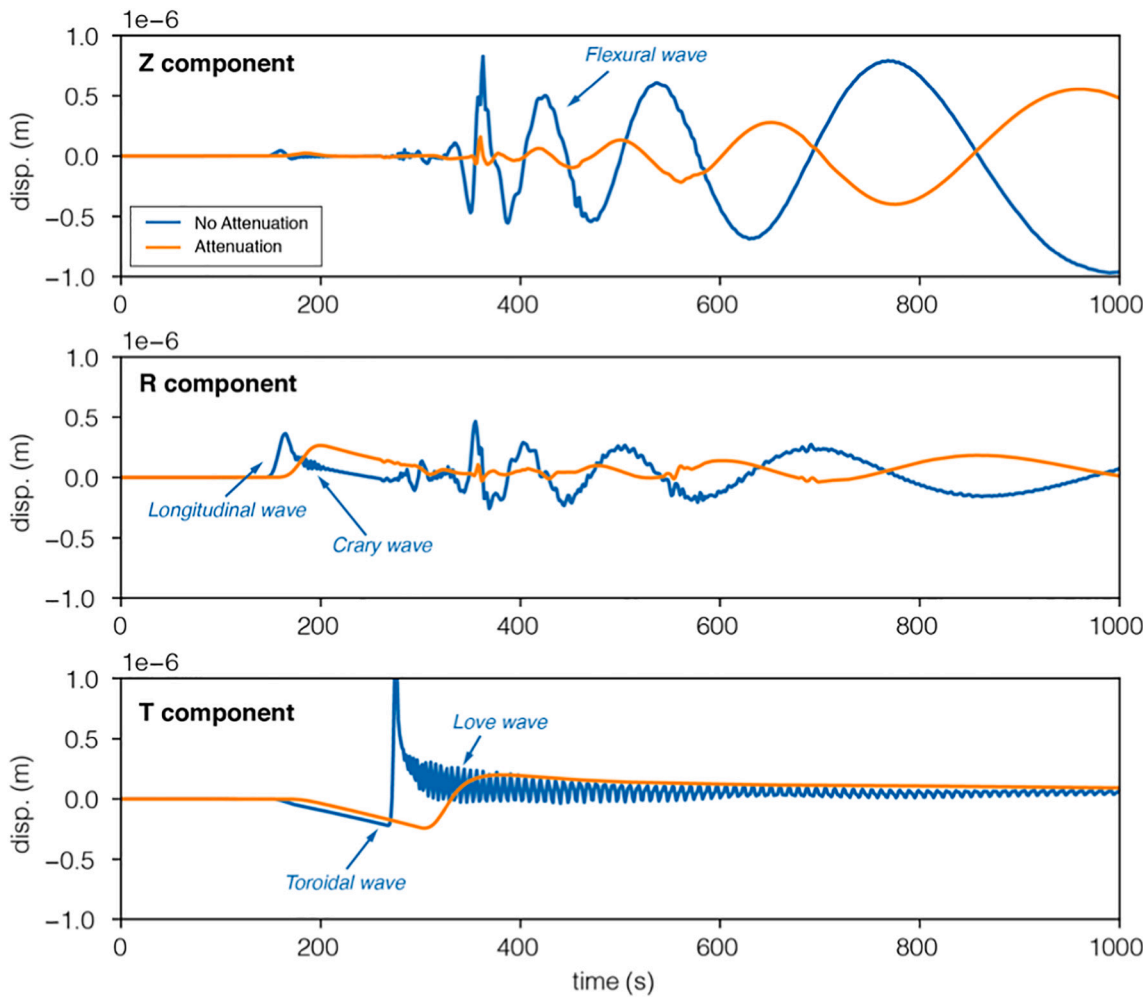


Fig. 3. Z (top), R (middle), and T (bottom) component synthetic seismograms calculated assuming a Mw 3 normal-faulting source at an epicentral distance of 20 degrees, for a 10 km thick ice shell. The orange and blue lines show synthetics calculated for models that include and neglect attenuation, respectively. Major seismic phases traveling in the ice shell are labeled.

et al., 1969). In this analysis, we window the vertical component synthetics around the Rayleigh and flexural wave train and pass the signal through a bank of narrow bandpass filters. The travel time for a given period is measured by picking the peak of the envelope of the waveform filtered at the corresponding center frequency. The travel time is then converted to group velocity using the epicentral distance. When the analysis is well behaved, the group velocity dispersion curve is extracted by following the ridge of the dispersion plot, where each column in the plot corresponds to the envelope of the filtered waveform. For the majority of our group velocity measurements, this procedure yields smooth dispersion curves. However, in some cases, most notably for measurements made at large epicentral distances, sharp jumps in the dispersion curve may be apparent. In these situations, we smooth the dispersion curve by fitting a cubic spline function to the observations. Practically, measurements of dispersion curves from European seismic data could be aided by prior knowledge about the expected functional shape (e.g., Fig. 8).

Fig. 4 shows the dispersion analysis performed for ice shell structures ranging from 5 to 20 km and for different assumptions about attenuation. In all cases, we use a Mw 3 event measured at 20 degrees epicentral distance. In each panel, we show the dispersion plot and the corresponding synthetic displacement waveform at its right. The extracted group velocity dispersion curve is drawn as a black line that follows the peak amplitude at each period. Additionally, we show the predicted fundamental mode group velocity dispersion curve for the given

structure, which we calculate using the normal mode summation code Mineos (Masters et al., 2011). For the case of a relatively thin 5 km ice shell with high attenuation (Fig. 4A), the measured group velocity dispersion curve closely matches the theoretical fundamental mode group velocity across the entire range of periods considered (between 5 and 250 s). However, for thicker ice shells, the group velocities measured at short period diverge from theoretical predictions. For example, in the case of a highly attenuating 10-km thick ice shell (Fig. 4B), the measured group velocity diverges from the predicted fundamental mode dispersion curve for periods shorter than about 25 s. In this range, the measured group velocities are faster than predicted by up to 25%.

There are two factors that complicate measurements of group velocity at short period. First, attenuation preferentially reduces the short period energy, thus making the short period end of the dispersion curve difficult to constrain. If attenuation is neglected for the same ice shell thickness (Fig. 4C), we see a close similarity between the measured and predicted group velocity dispersion curves, although there is still a divergence at the shortest periods (< 10 s). The divergence at short period is more pronounced for a 20 km thick ice shell, even when attenuation is neglected (Fig. 4D). Second, energy from higher order spheroidal mode branches (i.e., overtones) arrives coincidentally with the fundamental mode branch. Due to this interference, the short period end of the dispersion curve may be biased towards higher velocities. This is demonstrated in Fig. 5, where we show an example of vertical

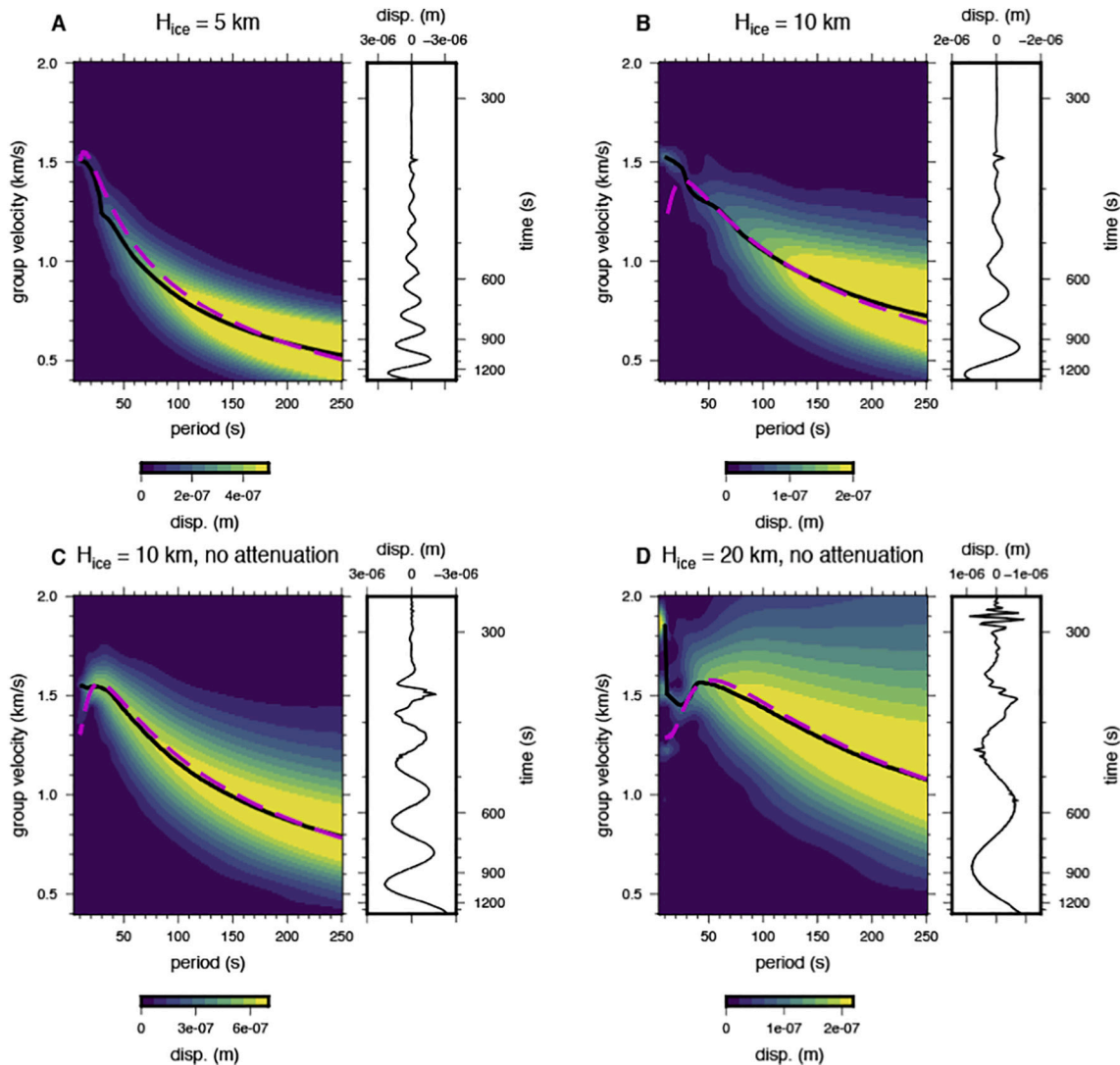


Fig. 4. Measurements of group velocity dispersion using the multiple filter technique for ice shell thicknesses ranging from 5 to 20 km. Each column of the dispersion plots represents the envelope of the waveform (shown to the right of the plot) filtered at the corresponding center frequency. The black line is the measured group velocity determined by the maximum of each envelope function. The pink dashed line is the dispersion curve predicted from Mineos. All dispersion measurements are made at 20 degrees epicentral distance.

component Mineos synthetics calculated for the fundamental mode spherical mode ($n = 0$), and the first three overtones ($n = 1, 2, 3$). The overtone branches contain relatively high frequency energy that is comparable in amplitude to the fundamental mode branch energy. The overprinting of this high frequency energy on the fundamental mode branch can mask the characteristic bend in the dispersion curve. To avoid these setbacks, we suggest inversions based on fundamental mode group velocity dispersion should be limited to periods of 25 s and above, where the group velocity of the fundamental mode branch can be accurately measured. In this study, we focus on inversions in the period range of 25–250 s.

If Love waves can be observed on Europa, their dispersion may also be useful for determining ice shell thickness (e.g., Kovach and Chyba, 2001). The Love wave in the ice exhibits a dispersive group velocity U according to

$$U(f) = \frac{V_{SICE}}{\sqrt{1 - \left(\frac{nV_{SICE}}{2fH_{ICE}}\right)^2}} \quad (1)$$

where f is frequency, n is order, H_{ICE} is ice shell thickness, and V_{SICE} is the

shear velocity in the ice shell. In the case where $n = 0$, the energy travels as a non-dispersive Toroidal wave with group velocity equal to V_{SICE} . An example of Love wave dispersion analysis for a 10 km thick ice shell is shown in Fig. 6. The source and receiver locations are the same as used in the analysis in Fig. 4. As before, we extract the group velocity dispersion using the multiple filter technique, but we consider only periods between 5 and 30 s given the limited bandwidth of the Love wave energy. We also plot the predicted Love wave group velocity dispersion curve from Eq. (1). For the high attenuation end member (Fig. 6A) the Love wave is absent. In this case, the dispersion plot shows non-dispersive energy with a group velocity of approximately 2 km/s, which corresponds to the long period Toroidal wave arrival. On the other hand, when attenuation is neglected (Fig. 6B) the dispersive Love wave is present immediately following the Toroidal wave, and lasts for several hundred seconds. In this scenario, the Love wave and Toroidal wave energy is clearly separated in the dispersion plot, and the measured Love wave dispersion closely matches the theoretical predictions.

Constraining ice shell thickness with Love wave dispersion is advantageous since strong dispersion is apparent at relatively short periods, which would relax the requirement for a very broadband

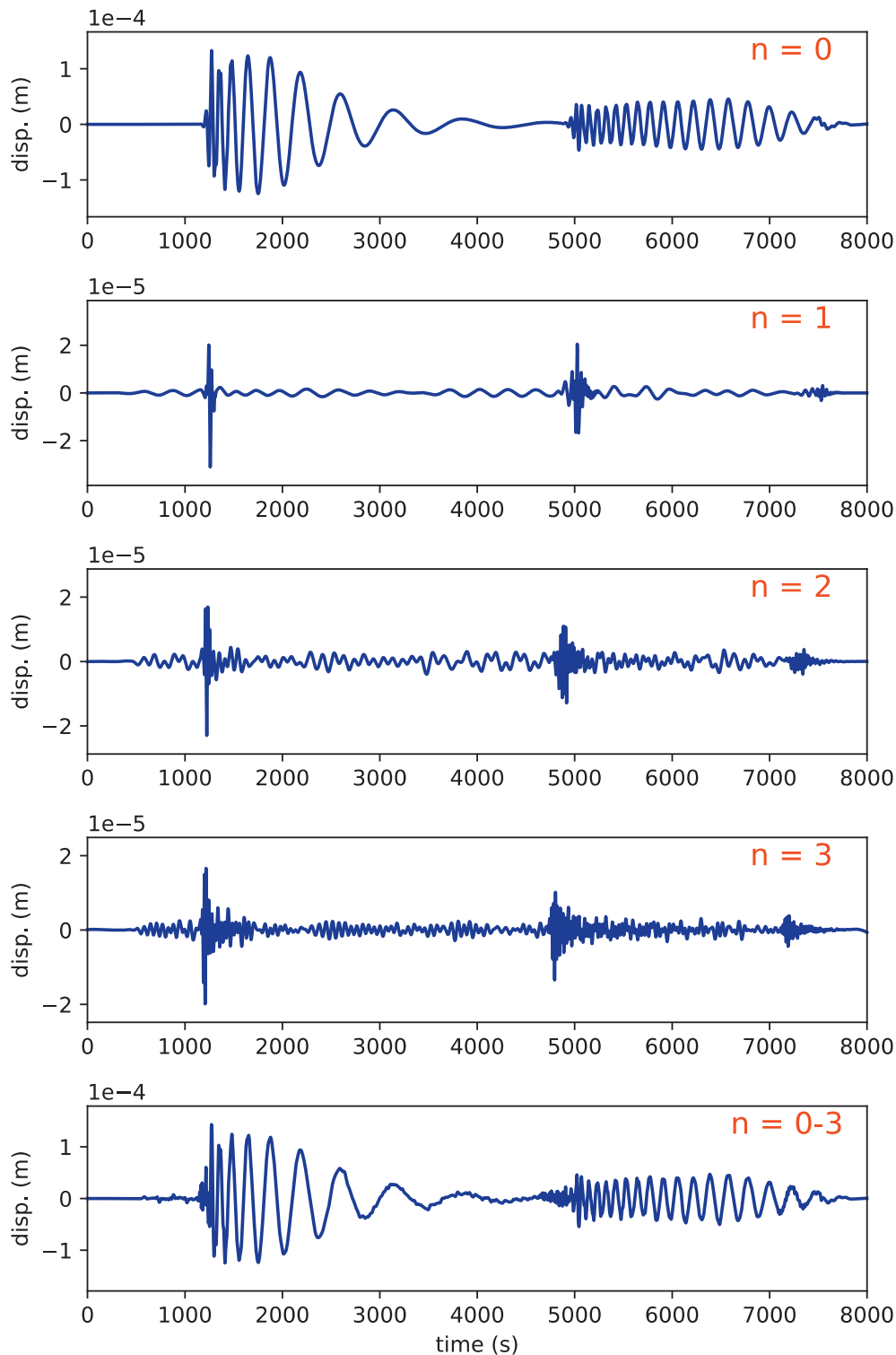


Fig. 5. Vertical component synthetics calculated from the fundamental spheroidal mode branch and its first three overtones. The top 4 panels show synthetics made from individual mode branches, and the bottom panel shows the combination of branches $n = 0$ to $n = 3$. Synthetics are computed using Mineos for a 20 km ice shell. The epicentral distance is 71.9 degrees, and the moment tensor represents a Mw 5.3 normal fault.

instrument. On the other hand, Love waves traveling in the ice shell may be difficult to identify if they are strongly attenuated, which our modeling suggests is likely at modest distances. However, if $Q\mu$ is significantly higher than in our ice shell models, Love wave dispersion could still provide a valuable constraint on ice shell thickness. In the remainder of this study, we focus on inverting dispersion curves of long period flexural waves since they appear to be dominant features in the

synthetic wavefields and should be clearly identifiable on the vertical component. Our approach could be easily adapted to invert Love wave dispersion curves if they are apparent in real data.

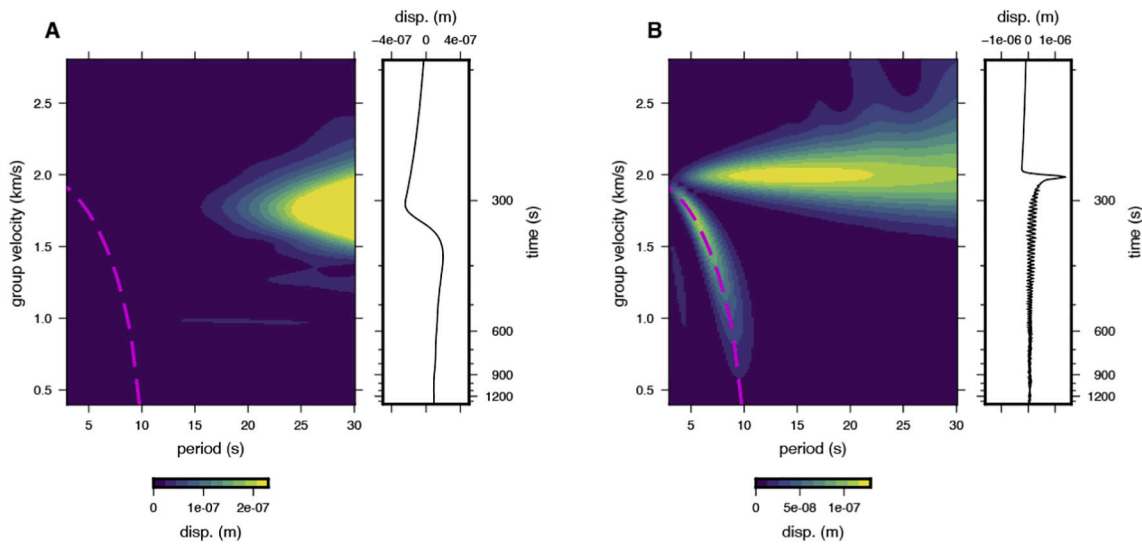


Fig. 6. Love wave dispersion analysis for a 10 km thick ice shell with attenuation considered (A) and neglected (B). In both cases, the source-receiver distance is 20 degrees and a Mw 3 source is used. The pink dashed line is the Love wave dispersion predicted using Eq. (1). The non-dispersive energy traveling with a group velocity of approximately 2 km/s is the Toroidal wave.

3. Inversion for ice shell thickness

3.1. Markov chain Monte Carlo inversion

To recover ice shell thickness, we measure Rayleigh and flexural wave group velocity dispersion from vertical component AxiSEM synthetics and invert the resulting dispersion curves using a Bayesian Markov chain Monte Carlo (McMC) approach (e.g., Sambridge and Mosegaard, 2002), which is efficient for low dimensional non-linear inverse problems. We choose a simple 2-layer model parameterization for the ice shell, comprised of a regolith layer with thickness H_{REG} and shear velocity V_{SREG} , and a coherent ice layer below with a fixed V_p , V_s , and density of 4 km/s, 2 km/s, and 1000 kg/m³. The total thickness of the ice is H_{ICE} . Below the ice shell, we include a subsurface ocean that extends to the silicate mantle, which is fixed at 127 km depth. While the structural models used for waveform simulations do not include a regolith layer, it is likely that a low velocity and potentially highly scattering layer could exist in the shallow subsurface of Europa, thus we explore the sensitivity of our inversion to this layer.

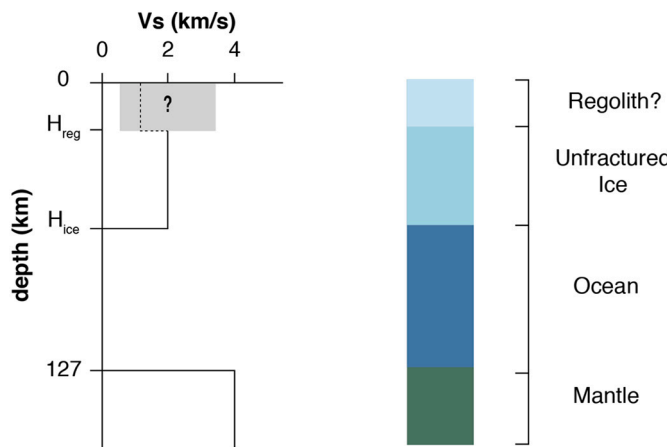


Fig. 7. Model parameterization which includes a 2 layer ice shell. The thickness and velocity of the top regolith layer is allowed to vary. The shear velocity of the bottom ice layer is fixed at $V_s = 2$ km/s and the depth to the mantle is fixed at 127 km. Below the water layer, we adopt the mantle and core structure from the models of Cammarano et al. (2006).

The structural model parameterization is shown in Fig. 7. We assume uniform priors for H_{REG} (between 0 km and 2 km), V_{SREG} (between 0.5 km/s and 2.0 km/s), and H_{ICE} (between 1 and 100 km). In both ice layers the V_p/V_s ratio is assumed to be 2, the density is fixed at 934 kg/m³, and the shear attenuation quality factor is fixed at $Q\mu = 100$. Our choice of $Q\mu$ is based the approximate average of $Q\mu$ in the 10 km thick ice shell for the high attenuation endmember case. Since the group velocity dispersion measurement depends on the epicentral distance Δ which may be poorly constrained, we treat it as a free parameter in the inversion, and assign it a uniform prior between 1 and 90 degrees. Thus, we have a 4-parameter inverse problem that consists of finding the optimal values of H_{ICE} , H_{REG} , V_{SREG} , and Δ .

Bayes theorem states that the posterior model distribution $P(\mathbf{m} | \mathbf{d})$ for a given a set of observations \mathbf{d} is proportional to the prior model distribution $P(\mathbf{m})$ multiplied by the likelihood function $P(\mathbf{d} | \mathbf{m})$, i.e.,

$$P(\mathbf{m} | \mathbf{d}) \propto P(\mathbf{m})P(\mathbf{d} | \mathbf{m}) \quad (2)$$

The likelihood function describes the probability that the model vector \mathbf{m} could produce the observed data. The form of $P(\mathbf{d} | \mathbf{m})$ depends on the choice of misfit function $\phi(\mathbf{m} | \mathbf{d})$, which defines the difference between the data and model predictions. Here, we choose a least squares misfit

$$\phi(\mathbf{m} | \mathbf{d}) = \left\| \frac{g(\mathbf{m}) - \mathbf{d}}{\sigma_d} \right\|^2 \quad (3)$$

where $g(\mathbf{m})$ is the forward problem, and σ_d is the standard error on the measurements. The likelihood function is then.

$$P(\mathbf{d} | \mathbf{m}) = \exp\left(\frac{-\phi(\mathbf{m} | \mathbf{d})}{2}\right) \quad (4)$$

In the McMC approach, $P(\mathbf{d} | \mathbf{m})$ is probabilistically sampled by drawing random realizations of \mathbf{m} from the prior distributions, and accepting or rejecting the model based on the likelihood function. Here, we adopt the Metropolis-Hastings algorithm for sampling the model space. The final ensemble of accepted solutions approximates the posterior. At each iteration of the McMC inversion, we propose a model vector \mathbf{m} , which consists of H_{ICE} , H_{REG} , V_{SREG} , and Δ . The model is proposed by randomly drawing from the prior distributions of each model parameter. The forward problem $g(\mathbf{m})$ is then to predict the fundamental mode dispersion curve for the proposed model, which we

solve using Mineos. In Fig. 8, we show Mineos predicted dispersion curves for homogeneous single-layer ice shell structures with thicknesses ranging between 5 and 100 km. The clear trend is that thin ice shells show more dispersive behavior. Additionally, the group velocity dispersion curves exhibit a characteristic bend (i.e., local maximum).

The inversion of group velocity dispersion curves is complicated by the fact that the group velocity measurement itself depends on knowing both the event distance and origin time. Thus, in our approach, we require an initial estimate of both of these values. If a 3-component seismometer is available, travel times of Longitudinal (LL) and Toroidal (LQ) waves may be easy to identify based on their polarizations. The traveltime differential Δt between these two phases, or between Rayleigh and the Longitudinal wave may then serve as an estimation of distance. Once an estimate of epicentral distance is made, the event origin time can be estimated from the expected traveltime of observed surface wave phases. Fig. 9 shows Δt as a function of distance for R - LL (panel A) and LQ - LL (panel B) measured from AxiSEM synthetics for ice shell structures ranging between 5 and 20 km thick. At short distances, Δt is not strongly dependent on ice shell structure, suggesting it would be a reasonably accurate proxy for distance. At larger distances, Δt for both R - LL and LQ - LL can be as large as 200 s or more.

The steps to performing an inversion are then i) Identify any two surface wave arrivals (from either R, LL, or LQ) based on their polarization, and estimate the epicentral distance. ii) Use the epicentral distance to estimate an event origin time, assuming V_s in the ice shell of 2 km/s. iii) Using the event origin time and epicentral distance, measure the group velocity dispersion curve of the Rayleigh and flexural wave train. iv) Invert the group velocity dispersion curve using the McMC approach. To account for the fact that the initial origin time and distance estimates may be inaccurate, at each iteration of the McMC inversion we convert the group velocity curve to group traveltime using the randomly proposed epicentral distance. An optimal group traveltime is calculated by removing the mean of difference between the predicted and observed group traveltime. The optimal group traveltime is then used to calculate the misfit function. As a result, this means that the initial estimate of the epicentral distance and origin time do not need to be accurate in order to yield accurate estimates of ice shell thickness. This is due to the fact that the predominant effect of choosing an incorrect initial estimate of epicentral distance is to shift the whole dispersion curve upwards or downwards. In other words, the shape of the dispersion curve, rather than the absolute value of group velocity, is the key constraint on ice

shell thickness. Additionally, it means that the recovered value of epicentral distance is not meaningful because the inversion will always be biased towards the initial estimate that was used. This is because the baseline shift of the dispersion curves will be similar when the proposed epicentral distance is close to the initial estimate. The effect of the initial estimate of epicentral distance on the inversions is discussed further in Section 3.3.

3.2. Inversions with known parameters

We first investigated inversions of dispersion curves from events with known distances and structural models. In Fig. 10, we show inversion results for each of the dispersion curves shown in Fig. 4, which correspond to ice shell thicknesses ranging between 5 and 20 km and variable attenuation structures. To avoid issues with short period dispersion observations, we inverted synthetic dispersion curves between periods of 25–250 s. In each case, the synthetics were calculated for a Mw 3 event at 20 degrees epicentral distance. The data uncertainty σ on group velocity observations was assumed to be 0.5 km/s. The posterior model parameter distributions are shown after 100,000 iterations. In all cases ice shell thickness is recovered to within one standard deviation of the true value (top left histogram of Fig. 10A–D). In general, the uncertainty of H_{ICE} increases with ice shell thickness, likely because the predicted group velocity dispersion curves become more similar to one another for thick ice shells. While the posteriors of both H_{ICE} and Δ are roughly Gaussian with clearly defined maxima, the posteriors of H_{REG} and V_{SREG} closely match the initial uniform prior distributions. This suggests that the inversions are not able to constrain the velocity structure in the upper 2 km of the ice shell where a regolith layer might be present.

In the examples shown in Fig. 10, the dispersion curves were calculated using the true distance and origin time. Thus, these inversions should be considered the most favorable scenarios. Next, we explored scenarios in which the epicentral distance was estimated from travel time differentials of R and LL. For ice shell thicknesses between 5 and 40 km, we made dispersion measurements from synthetics calculated for a Mw 3 event at distances ranging between 10 and 40 degrees. While there is no clear limit to the distance at which group velocity dispersion measurements can be made, we note that with increasing distance it may be increasingly difficult to constrain the short period end of the dispersion curve due to the effect of attenuation. Additionally, for thick ice shells, flexural waves become more difficult to identify with increasing distance. For example, in the case of a 40 km thick ice shell,

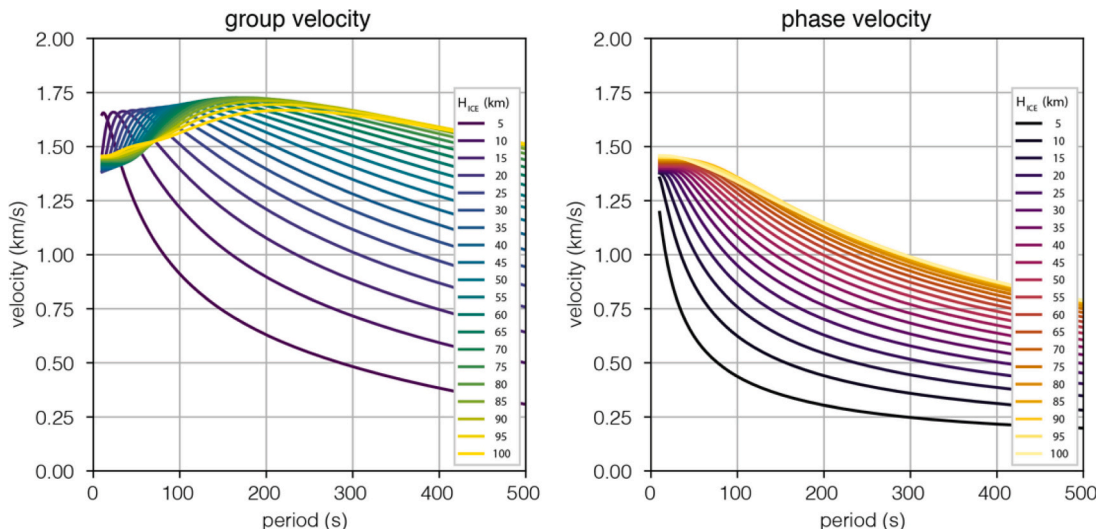


Fig. 8. Group velocity (left) and phase velocity (right) dispersion curves calculated for Europa structural models with ice shell thicknesses ranging from 5 to 100 km, predicted using Mineos. The shear velocity in the ice layer is $V_s = 2$ km/s. Longer periods travel slower because they are more sensitive to the subsurface ocean.

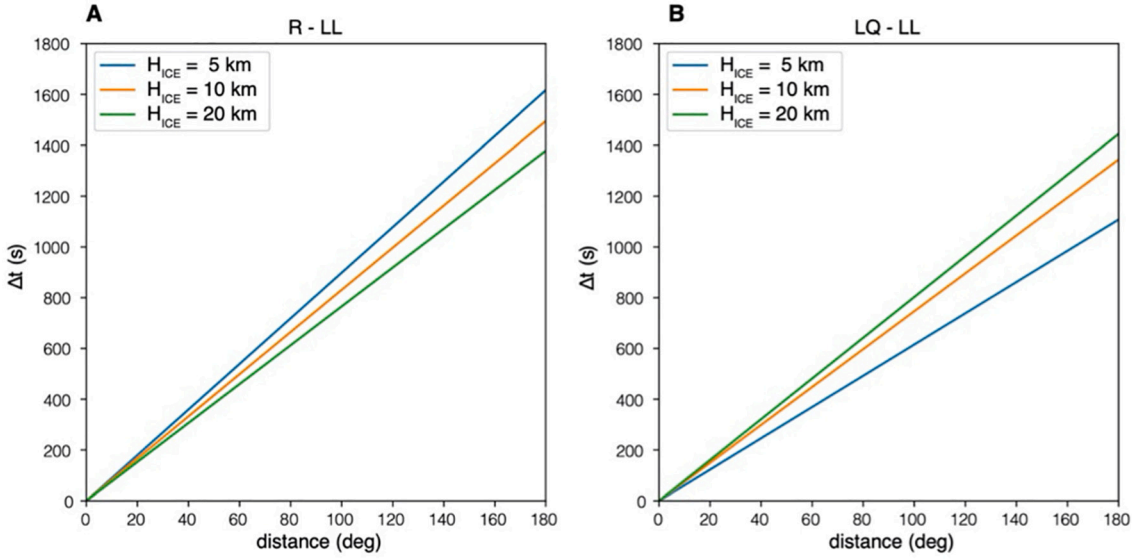


Fig. 9. Travel time differentials between surface wave phases R and LL (Panel A) and LQ and LL (Panel B), calculated for different ice shell thicknesses.

no clear dispersive flexural wave was apparent at distances greater than approximately 50 degrees. Thus, here we focus on relatively close events, which we assume will be the most likely to be observed during the timeframe of a Europa lander mission. In each case we approximate the epicentral distance from the R – LL time using Δt predicted for a 10 km thick ice shell model (Fig. 8A). LL picks are made on the maximum of the first clear arrival on the radial component, and R picks are made at the onset of the Rayleigh wave train on the vertical component (see Figs. SI1–SI4). Since we have shown that the inversions are insensitive to the shallowest subsurface structure, from here on we neglect H_{REG} and V_{SREG} and invert for only H_{ICE} and Δ using a grid search approach, which is efficient for low dimensional inverse problems. However, we note that with real data, the McMC approach may still be advantageous because it is more adaptable to alternative model parameterizations.

Table 1 summarizes results for ice shell thicknesses ranging from 5 to 40 km, and for dispersion measurements made at epicentral distances between 10 and 40 degrees. In general, the epicentral distance estimated from R – LL (Δ_{EST}) gives a close approximation (less than 5 degrees difference) of the true distance (Δ_{TRUE}), regardless of the ice shell thickness. In all scenarios where the ice shell is 20 km thick or less, the mean of H_{ICE} is within 1.7 km of the true value, which we consider to be well recovered. In the case of a 40 km thick ice shell, the mean of H_{ICE} underestimates the true ice shell thickness by at least 10 km for all distances considered. Again we see that the uncertainty on H_{ICE} increases with ice shell thickness. For a 5 km thick ice shell, the standard deviation is 1.5 km or less for all distances, while the standard deviation is as large as 11.4 km for a 40 km thick ice shell. The underestimation of H_{ICE} for thick ice shells can likely be attributed to poorly constrained dispersion measurements, and the large uncertainty is due to the fact that the forward predicted dispersion curves become increasingly similar for thick ice shells. Additionally, choices made in the model parameterization, such as $Q\mu$ in the ice shell, could have an effect on the recovered values, although we found the effect is minimal. For example, in Table S1 we investigate how the value of $Q\mu$ affects the recovered ice shell thickness. For thin ice shells (20 km or less), $Q\mu$ does not have a strong effect on H_{ICE} , although slightly thicker (typically ~ 1 – 2 km) ice shells are recovered when assuming a low attenuation of $Q\mu = 10$. The effect is more dramatic for a 40 km thick ice shell, where reducing $Q\mu$ can increase the recovered ice shell thickness by roughly 4 km.

3.3. Effect of initial epicentral distance and origin time estimates

While accurate measurements of group velocity dispersion, which could be useful for understanding ice shell properties, depend on accurate measurements of epicentral distance, our inversion scheme can in principle recover ice shell thickness even without knowing the correct epicentral distance. To demonstrate this, we performed a test in which a synthetic seismogram calculated for a 5 km thick ice shell was inverted using both the correct and incorrect epicentral distance (Fig. 11). When the correct distance was used (here, 20 degrees), the dispersion curve yields accurate values of the frequency dependent group velocity of flexural waves in the ice shell. When an inaccurate distance was used (here, 10 degrees) the estimated origin time shifts, and the values of the dispersion curve are no longer accurate (Fig. 11B). However, since the shape of the dispersion curve is the key constraint on the ice shell thickness, the dispersion curve estimated from an inaccurate epicentral distance can still be used successfully in the inversion. This is demonstrated in Fig. 11C and D, which show the grid search results for the case of the correct and incorrect epicentral distances respectively. In both cases, the mean of H_{ICE} is well recovered (within 0.4 km of the true thickness), although the uncertainty is slightly larger in the case where the incorrect distance was used ($H_{ICE} = 5.2 \pm 1.6$ km compared to $H_{ICE} = 5.4 \pm 0.7$ km). While here we show a scenario where the true epicentral distance was underestimated, our tests show that the inversions can also work when the epicentral distance is overestimated. Additionally, we note that the values of the group velocity dispersion curve can be used as a diagnostic to tell whether the estimated epicentral distance is reasonable. In this case, assuming an epicentral distance of 10 degrees yields a group velocity of over 2.5 km/s at short periods, which is unrealistically fast. In practice, when making the measurement, the epicentral distance should be tuned such that the peak group velocity is lower than roughly 2 km/s.

3.4. Blind inversions

As a further test, we applied our inversion approach to events from Panning et al. (2018)'s preferred synthetic Europa seismicity catalog (see Section 2.2 for a description of the seismicity model). We considered two catalogs from Panning et al. (2018) that were calculated for structural models with either a 5 km or 20 km thick ice shell. The structural model in the 5 km thick ice shell scenario also included scattering in the ice shell, which was described as a von Karman random

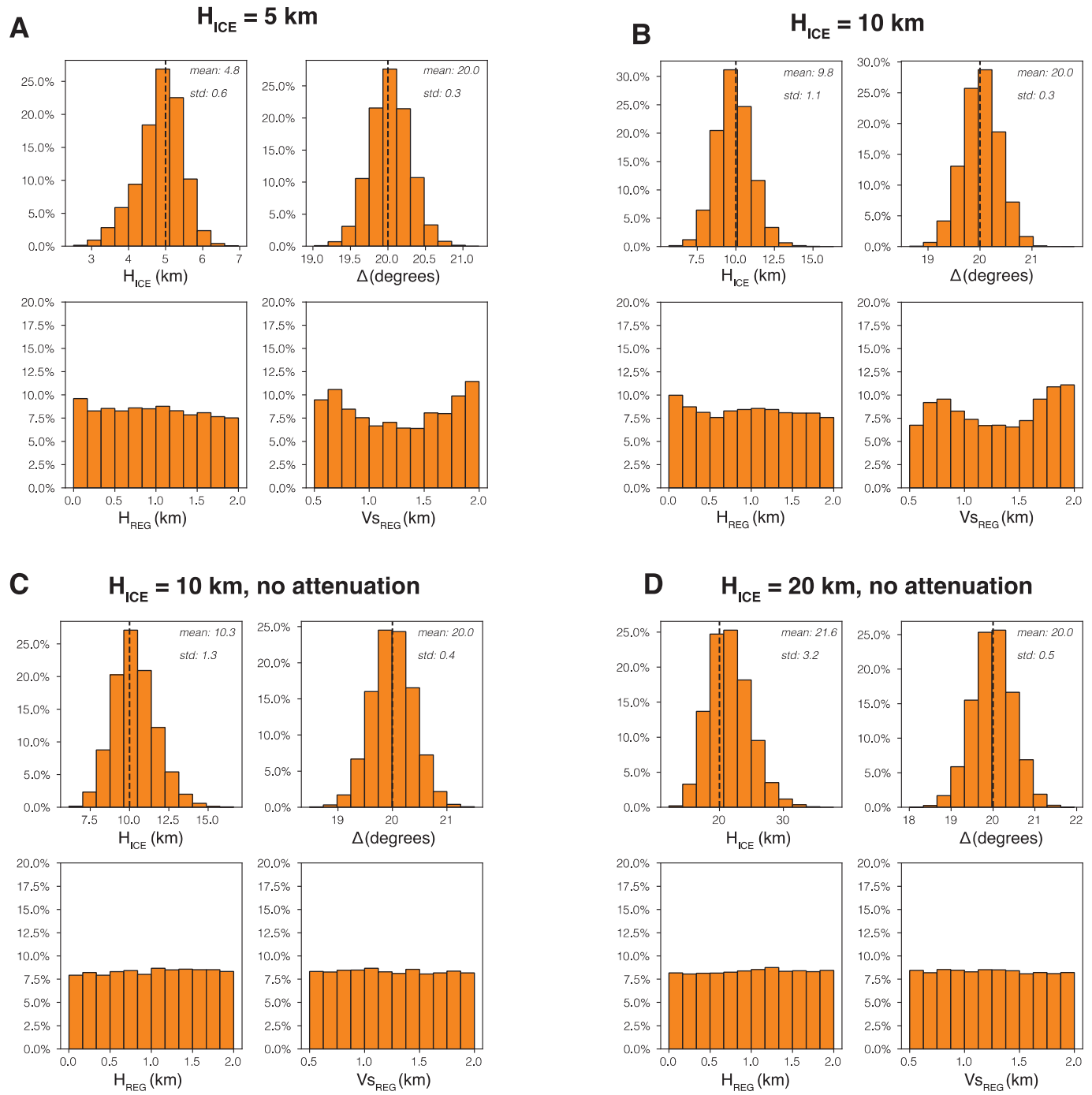


Fig. 10. Posterior distributions of McMC inversions. Results are shown for a 5 km thick anelastic ice shell (A), a 10 km thick anelastic ice shell (B), a 10 km thick elastic ice shell (C), and a 20 km thick elastic ice shell (D). The event distance in all cases is 20 degrees. The vertical dashed lines show the true model parameters. All inversions are performed using the period range 25–250 s.

medium with velocity perturbations of $\pm 10\%$ and a correlation wavelength of 5 km. The 7-day synthetic records, which contain both events and noise, are shown in Fig. 12. We consider this “blind” test to be the closest feasible approximation to performing an inversion on real seismic data from Europa since we do not know the event locations, origin times, or source properties that were used to construct the synthetic dataset. However, we note that it is not a true blind inversion because we know the ice shell thickness beforehand.

We selected one event from both synthetic catalogs that fit our criteria of i) having a clear long period flexural wave apparent on the vertical component, ii) having a peak vertical displacement of greater

than $1 \times 10^{-8} \text{ m}$, iii) having a clear LL arrival on the radial component, and iv) having a relatively close epicentral distance (< 50 degrees). The selected events for each catalog are shown in Fig. 12(B and D). In the 5 km and 20 km thick ice shell scenarios, R – LL times of 159 s and 277 s yield initial epicentral distance estimates of 19.0 degrees and 33.0 degrees respectively. Group velocity dispersion measurements are made at periods between 25 and 250 s (Fig. S5). As in previous inversions, we assume a homogeneous ice layer with $Vs_{\text{ICE}} = 2 \text{ km/s}$ and $Vp_{\text{ICE}} = 4 \text{ km/s}$, and $Q\mu = 100$. In both cases, the true ice shell thickness is well recovered, although the mean of the posterior distributions slightly underestimates the true ice shell thickness in both scenarios (Fig. 13).

Table 1

Summary of inversion results for 5–40 km thick ice shells.

Input Model	Δ_{TRUE} (deg)	R – LL (s)	Δ_{EST} (deg)	H_{ICE} (km)	Δ (deg)
5 km	10	90	10.8	5.1 ± 1.5	10.7 ± 0.3
5 km	20	184	22.0	5.7 ± 1.4	22.1 ± 0.6
5 km	40	374	44.8	5.1 ± 1.5	44.6 ± 1.5
10 km	10	90	10.8	11.7 ± 3.9	10.7 ± 0.5
10 km	20	173	20.7	11.2 ± 3.6	20.6 ± 0.9
10 km	40	340	40.7	11.1 ± 3.0	40.5 ± 1.4
20 km	10	86	10.3	20.4 ± 7.1	10.1 ± 0.5
20 km	20	169	20.3	19.4 ± 6.0	20.4 ± 1.0
20 km	40	350	41.9	18.3 ± 5.4	41.9 ± 1.8
40 km	10	85	10.2	$29.9 \pm$ 11.4	10.1 ± 0.7
40 km	20	170	20.4	$28.5 \pm$ 10.0	20.3 ± 0.9
40 km	40	314	38.8	$28.7 \pm$ 11.1	38.4 ± 2.5

Δ_{TRUE} is the true epicentral distance of the synthetics, and Δ_{EST} is the epicentral distance estimated from the travel time differential between the Rayleigh wave and Longitudinal mode ($R - LL$). The recovered model parameters H_{ICE} and Δ are given with uncertainties.

4. Discussion

In practice, constraining Europa's ice shell thickness from Rayleigh and flexural wave dispersion would require the development of a broadband seismometer suitable for the harsh surface conditions of Europa, and which is sensitive enough to record long period (10's to 100's of seconds) vertical surface deformations expected from relatively

small events (< Mw 5). To estimate the required sensitivity, we show the displacement power spectra for events with magnitudes between Mw 1 and Mw 5 at epicentral distances of 20 degrees and 90 degrees (Fig. 14). The synthetics were calculated for a 5 km thick ice shell using the high attenuation scenario. For comparison, we plot the noise floor of two broadband instruments commonly used in terrestrial seismology; the Nanometrics Trillium Compact, and the Streckeisen STS2. At 20 degrees epicentral distance flexural waves from a Mw 3 event would be roughly 5–25 dB above the noise floor of an STS2-like instrument at all periods used in the inversions in this study. On the other hand, at 90 degrees epicentral distance, only periods below about 20 s would be above the noise floor of the STS2 for a Mw 3 event. In the case of a Mw 5 event at 90 degrees, periods above 100 s would only be several dB above the noise floor of the Trillium Compact, but would be well resolved with the STS2. Since the flexural wave amplitudes diminish with increasing ice shell thickness, a thicker ice shell would impose even stricter sensitivity requirements to observe flexural waves. Thus, the inversion method we propose would be most feasible on Europa if a broadband seismometer comparable to the most sensitive seismic instruments used in terrestrial seismology were developed for a Europa lander mission.

Short period dispersion measurements could be useful at constraining Europa's internal ice shell structure, although this would rely on accurately locating seismic events which is challenging when only a single station is available. Here, we used the travel time differentials between surface wave phases with clear polarizations as an estimate for distance, but it is not clear how well this may work on actual data. Ideally, a sparse seismic network could be employed to accurately locate seismic events on Europa, but realistically any future lander mission will be limited to a single station. While unlikely, it is possible that precise

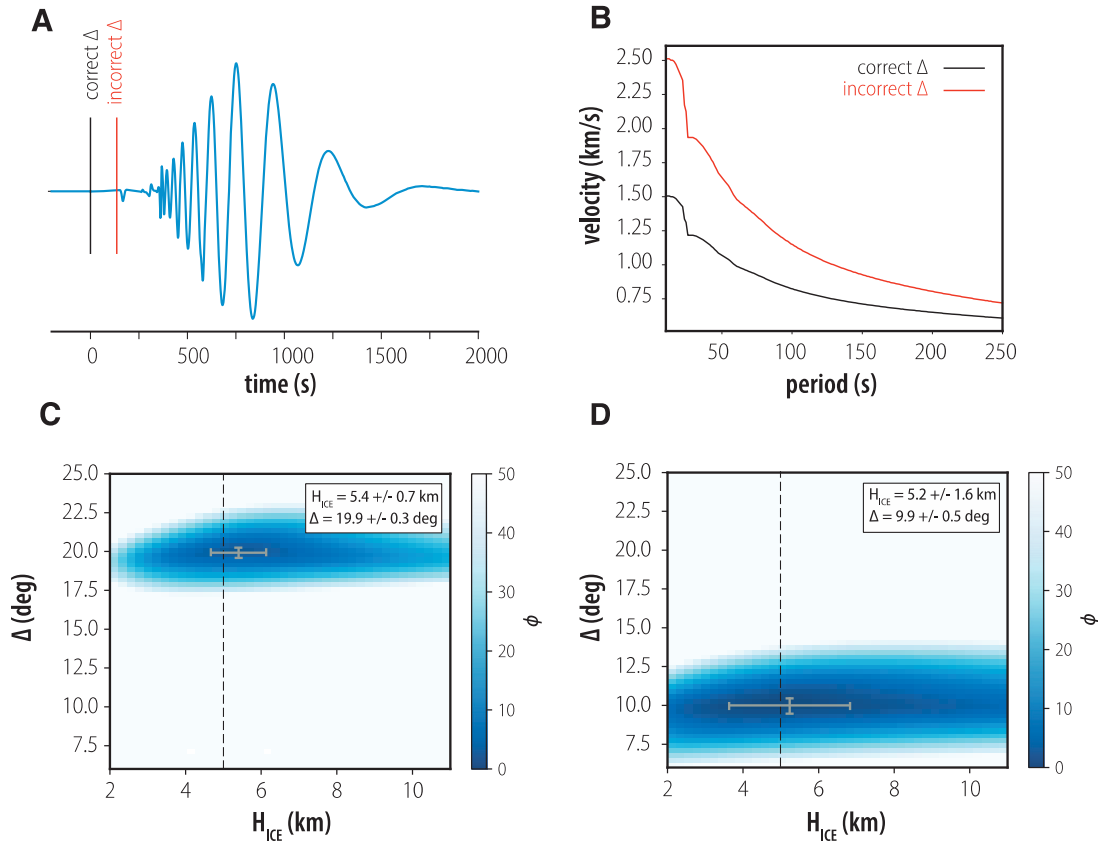


Fig. 11. Effect of initial estimate of epicentral distance and origin time on inversion results. Panel A shows the vertical component displacement seismogram, calculated for a 5 km thick ice shell. The true epicentral distance is 20 degrees. Black and red vertical lines show the estimated origin times for an assumed epicentral distance of 20 degrees and 10 degrees respectively. The corresponding group velocity dispersion curves are shown in Panel B. The inversion results that used the correct epicentral distance are shown in C, and the inversion results that used the incorrect epicentral distance are shown in D. In the top right of each panel, the mean and standard deviation of model parameters is shown, which correspond to the error bars shown in the plot.

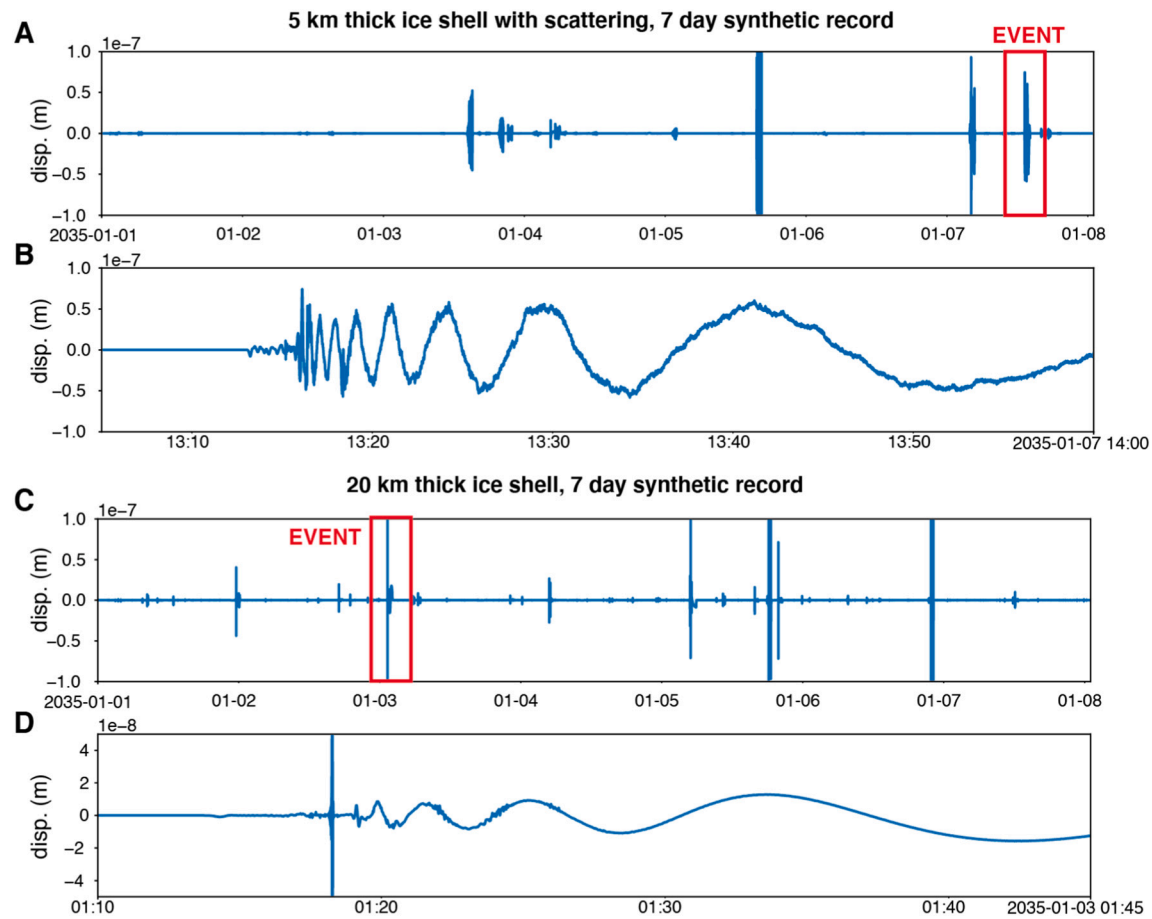


Fig. 12. 7-day synthetic records from the preferred Europa seismicity catalog of Panning et al. (2018). Panels (A) and (C) show the vertical displacement records for a 5 km thick ice shell and a 20 km thick ice shell, respectively. Panels (B) and (D) show a zoom-in on the events selected for inversion.

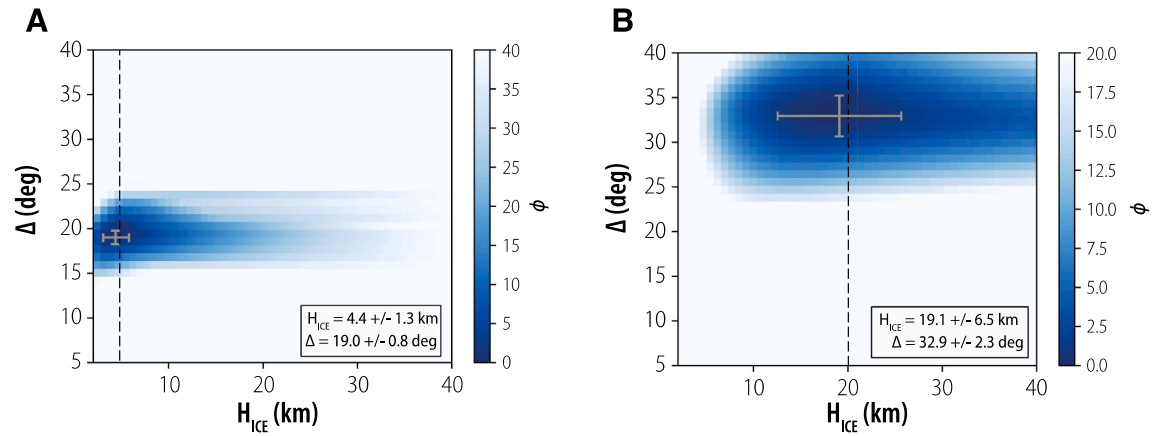


Fig. 13. Results of blind inversions for the 5 km thick ice shell (panel A) and 20 km thick ice shell (panel B). Vertical dashed lines show the true ice shell thickness.

event distances could be determined by linking recorded seismicity to new surface features that appear in satellite imagery (e.g., either new surface fractures or impact craters). For example, during the course of the InSight mission on Mars, a new 1.5 m diameter crater was excavated from an impact approximately 37 km away from the seismometer, but no signal was definitively identified in the data (Daubier et al., 2020). Tsuji and Teanby (2016) estimated that large impacts that generate waves observable on regional to global scales are exceedingly rare on Europa, with between 10^{-8} and 1 impact expected per year. Therefore, they should not be considered a reliable source of seismicity for a Europa

seismic lander.

Our simulations of seismic wave propagation assume simple radially symmetric (i.e. 1D) models of Europa's interior structure, yet the ice shell may not have a uniform thickness. For example, the ice shell of Enceladus is expected to be highly variable in thickness, with the thinnest ice underlying the south polar region (e.g., Hemingway et al., 2018). 3D seismic modeling of Europa's ice shell structure (Tharimena et al., 2019) suggests that flexural waves are still apparent in ice shells with long wavelength variations in thickness. In this case the measured surface wave velocity dispersion is related to the path averaged ice shell

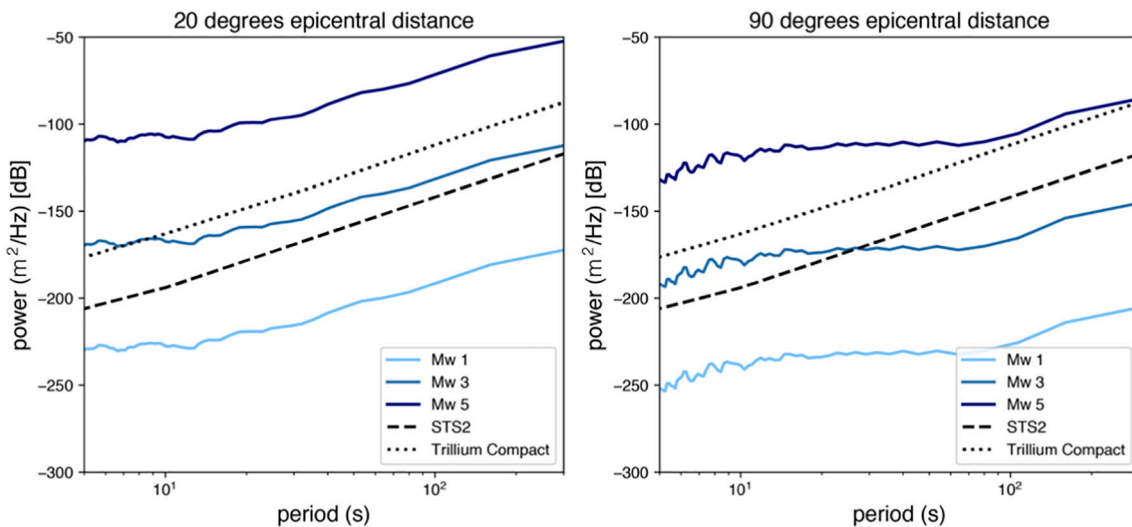


Fig. 14. Displacement power spectra of synthetics calculated for a 5 km thick ice shell, for events at a distance of 20 degrees (left), and 90 degrees (right). The noise floor of the Trillium Compact and STS2 seismometers are shown for comparison.

thickness. In the normal mode formalism, lateral heterogeneity induces mode coupling. Accounting for this coupling along a branch is equivalent to making the assumption that the dispersion represents path-averaged structure between source and receiver (e.g., Romanowicz, 1987). This assumption is a good one when the fundamental branch is well-isolated from other branches (in frequency-wavenumber space), which is likely to be the case for long period fundamental mode surface waves considered here. Additionally, we note that our waveform simulations are based on a purely viscoelastic formulation of the wave equation, and thus does not explicitly account for the effects of gravity, which could influence long period flexural wave amplitudes. However, we find that the effect is negligible for the periods considered here (< 250 s) (Fig. S6).

5. Conclusions

We performed a set of synthetic seismic experiments aimed at understanding how well a 3-component broadband station on Europa could recover ice shell thickness using surface wave dispersion. From synthetic seismograms, we measured group velocity dispersion of Rayleigh and flexural waves at long period and inverted the dispersion curves for ice shell structure using either an MCMC or grid search approach. We find that events with magnitude Mw 3 or greater, which may be common on Europa, generate flexural waves that could be observed at regional to teleseismic distances with broadband instruments comparable in sensitivity to those commonly used in terrestrial seismology. Inversions of group velocity dispersion curves in the period range of 25–250 s generally recover ice shell thickness to within several km for epicentral distances ranging between 10 and 40 degrees. With increasing epicentral distance and ice shell thickness, group velocity dispersion curves are more difficult to measure since flexural waves in thick ice shells have smaller amplitudes and exhibit less dispersion. Thus, flexural wave inversion is most likely to be successful in the case of thin ice shells (< 40 km). We suggest that a seismic instrument onboard a future Europa lander mission should be sensitive to periods upwards of 200 s in order to enable inversions of flexural wave dispersion, which would provide complimentary constraints on ice shell thickness to those made from short period body wave observations. Finally, we found that while in principle Love wave dispersion may also be used to invert for ice shell thickness, accurate dispersion measurements in the period range of 5–30 s may be hindered if Europa's ice shell is highly attenuating.

Declaration of Competing Interest

None

Acknowledgements

We thank Mark Panning and an anonymous reviewer, as well as Editor-In-Cheif Rosaly Lopes, for helpful comments that have allowed us to improve this manuscript. RM and NS were supported by a NASA-COLDTECH grant #NNX17AF70G and NS also by NASA-PSTAR grant #80NSSC17K0229 and NASA SSERVI GEODES grant #80NSSC19M0216. Additionally, RM was supported in part by NSF postdoctoral fellowship Award #1806412.

Appendix A. Supplementary data

Supplementary data to this article can be found online at <https://doi.org/10.1016/j.icarus.2021.114617>.

References

- Bassis, J.N., Fricker, H.A., Coleman, R., Bock, Y., Behrens, J., Darnell, D., Okal, M., et al., 2007. Seismicity and deformation associated with ice-shelf rift propagation. *J. Glaciol.* 53 (183), 523–536. <https://doi.org/10.3189/002214307784409207>.
- Cammarano, F., Lekic, V., Manga, M., Panning, M., Romanowicz, B., 2006. Long-period seismology on Europa: 1. Physically consistent interior models. *J. Geophys. Res. E Planets* 111 (12), 1–11. <https://doi.org/10.1029/2006JE002710>.
- Carr, M.H., Belton, M.J.S., Chapman, C.R., Davies, M.E., Geissler, P., Greenberg, R., McEwen, A.S., et al., 1998. Evidence for a subsurface ocean on Europa. *Nature* 391 (6665), 363–365. <https://doi.org/10.1038/34857>.
- Cheng, C.H., Toksöz, M.N., 1978. Tidal stresses in the Moon. *J. Geophys. Res.* 83 (B2), 845. <https://doi.org/10.1029/jb083ib02p00845>.
- Compaire, N., Margerin, L., Garcia, R.F., Pinot, B., Calvet, M., Orland-Mainsant, G., Kim, D., et al., 2021. Autocorrelation of the Ground Vibrations Recorded by the SEIS-InSight Seismometer on Mars. *Journal of Geophysical Research: Planets* 126 (4), 1–20. <https://doi.org/10.1029/2020JE006498>.
- Crary, A.P., 1954. Seismic studies on Fletcher's ice island, T-3. *Trans. Am. Geophys. Union* 35 (2), 293–300.
- Daubar, I., Lognonné, P., Teamby, N.A., Collins, G.S., Clinton, J., Stähler, S., Spiga, A., et al., 2020. A New Crater Near InSight: Implications for Seismic Impact Detectability on Mars. *J. Geophys. Res. Planets* 125 (8). <https://doi.org/10.1029/2020JE006382>.
- Dziewonski, A., Bloch, S., Landisman, M., 1969. A technique for the analysis of transient seismic signals. *Bull. Seismol. Soc. Am.* 59 (1), 427–444.
- Eluszwickiewicz, J., 2004. Dim prospects for radar detection of Europa's ocean. *Icarus* 170 (1), 234–236. <https://doi.org/10.1016/j.icarus.2004.02.011>.
- Golombek, M.P., Banerdt, B.W., Tanaka, K., Tralli, D.M., 1992. A prediction of Mars seismicity from surface faulting. *Science* 258 (5084), 979–981.
- Greenberg, R., Geissler, P., Hoppa, G., Tufts, B.R., Durda, D.D., Pappalardo, R., Head, J. W., et al., 1998. Tectonic Processes on Europa: Tidal Stresses, Mechanical Response,

- and Visible Features. *Icarus* 135 (1), 64–78. <https://doi.org/10.1006/icar.1998.5986>.
- Guilia, L., Wiemer, S., 2010. The influence of tectonic regimes on the earthquake size distribution: a case study for Italy. *Geophys. Res. Lett.* 37 (10), 1–6. <https://doi.org/10.1029/2010GL043066>.
- Helmstetter, A., Moreau, L., Nicolas, B., Comon, P., Gay, M., 2015. Intermediate-depth icequakes and harmonic tremor in an Alpine glacier (Glacier d'Argentière, France): evidence for hydraulic fracturing. *J. Geophys. Res. Earth Surf.* 120 (3), 402–416. <https://doi.org/10.1002/2014JF003289>.
- Hemingway, D., Iess, L., Tajeddine, R., Tobie, G., 2018. The interior of Enceladus. In: *Enceladus and the Icy Moons of Saturn*. University of Arizona Press, pp. 57–77.
- Hoppa, G., Tufts, B., Greenberg, R., Geissler, P., 1999. Strike-slip faults on Europa: global shear patterns driven by tidal stress. *Icarus* 298, 287–298.
- Hurford, T.A., Henning, W.G., Maguire, R., Lekić, V., Schmerr, N., Panning, M., Bray, V. J., et al., 2019. Seismicity on Tidally Active Solid-Surface Worlds. *Icarus* 338. <https://doi.org/10.1016/j.icarus.2019.113466>.
- Kivelson, M.G., Khurana, K.K., Russell, C.T., Volwerk, M., Walker, R.J., Zimmer, C., 2000. Galileo magnetometer measurements: a stronger case for a Subsurface Ocean on Europa. *Science* 289, 1340–1343.
- Kovach, R.L., Chyba, C.F., 2001. Seismic detectability of a subsurface Ocean on Europa. *Icarus* 150 (2), 279–287. <https://doi.org/10.1006/icar.2000.6577>.
- Lam, T., Buffington, B.B., Campagnola, S., Scott, C., Ozimek, M., 2018. A robust mission tour for NASA's planned europa clipper mission. In: *Space Flight Mechanics Meeting*, 2018, (210009). <https://doi.org/10.2514/6.2018-0202>.
- Lammlein, D.R., 1977. Lunar seismicity and tectonics. *Phys. Earth Planet. Inter.* 14 (3), 224–273. [https://doi.org/10.1016/0031-9201\(77\)90175-3](https://doi.org/10.1016/0031-9201(77)90175-3).
- Lammlein, D.R., Latham, G.V., Dorman, J., Nakamura, Y., Ewing, M., 1974. Lunar seismicity, structure, and tectonics. *Rev. Geophys.* 12 (1), 1–21. <https://doi.org/10.1029/RG012i001p0001>.
- Lee, S., Zanolin, M., Thode, A.M., Pappalardo, R.T., Makris, N.C., 2003. Probing Europa's interior with natural sound sources. *Icarus* 165 (1), 144–167. [https://doi.org/10.1016/S0019-1035\(03\)00150-7](https://doi.org/10.1016/S0019-1035(03)00150-7).
- Masters, G., Woodhouse, J.H., Freeman, G., 2011. *Mineos – User Manual Version 1.0.2*.
- Nakamura, Y., 1977. HFT events: shallow moonquakes? *Phys. Earth Planet. Inter.* 14 (3), 217–223. [https://doi.org/10.1016/0031-9201\(77\)90174-1](https://doi.org/10.1016/0031-9201(77)90174-1).
- Nimmo, F., Schenk, P., 2006. Normal faulting on Europa: implications for ice shell properties. *J. Struct. Geol.* 28 (12), 2194–2203. <https://doi.org/10.1016/j.jsg.2005.08.009>.
- Nimmo, F., Giese, B., Pappalardo, R.T., 2003. Estimates of Europa's ice shell thickness from elastically-supported topography. *Geophys. Res. Lett.* 30 (5) <https://doi.org/10.1029/2002gl016660>.
- Nissen-Meyer, T., van Driel, M., Stähler, S.C., Hosseini, K., Hempel, S., Auer, L., Colombi, A., et al., 2014. AxiSEM: Broadband 3-D seismic wavefields in axisymmetric media. *Solid Earth* 5 (1), 425–445. <https://doi.org/10.5194/se-5-425-2014>.
- Oberst, J., 1987. Unusually high stress drops associated with shallow moonquakes. *J. Geophys. Res.* 92, 1397–1405.
- Panning, M., Lekic, V., Manga, M., Cammarano, F., Romanowicz, B., 2006. Long-period seismology on Europa: 2. Predicted seismic response. *J. Geophys. Res.* 111 (March 2006), 1–12. <https://doi.org/10.1029/2006JE002712>.
- Panning, M.P., Stähler, S.C., Huang, H.H., Vance, S.D., Kedar, S., Tsai, V.C., Pike, W.T., Lorenz, R.D., 2018. Expected seismicity and the seismic noise environment of Europa. *J. Geophys. Res.-Planets* 123 (1), 163–179. <https://doi.org/10.1002/2017JE005332>.
- Pappalardo, R.T., Belton, M.J.S., Breneman, H.H., Carr, M.H., Chapman, C.R., Collins, G. C., Denk, T., et al., 1999. Does Europa have a subsurface ocean? Evaluation of the geological evidence. *J. Geophys. Res. Planets* 104 (E10), 24015–24055. <https://doi.org/10.1029/1998JE000628>.
- Quick, L.C., Marsh, B.D., 2015. Constraining the thickness of Europa's water-ice shell: insights from tidal dissipation and conductive cooling. *Icarus* 253, 16–24. <https://doi.org/10.1016/j.icarus.2015.02.016>.
- Romanowicz, B., 1987. Multiplet-multiplet coupling due to lateral heterogeneity: asymptotic effects on the amplitude and frequency of the Earth's normal modes. *Geophys. J. Int.* 90 (1), 75–100.
- Sambridge, M., Mosegaard, K., 2002. Monte Carlo methods in geophysical inverse problems. *Rev. Geophys.* 40 (3) <https://doi.org/10.1029/2000RG000089>, 3–13–29.
- Sens-Schönfelder, C., Larose, E., 2010. Lunar noise correlation, imaging and monitoring. *Earthq. Sci.* 23 (5), 519–530. <https://doi.org/10.1007/s11589-010-0750-6>.
- Shirley, J.H., 1986. Shallow moonquakes and large shallow earthquakes: a temporal correlation. *Earth Planet. Sci. Lett.* 76 (3–4), 241–253. [https://doi.org/10.1016/0012-821X\(86\)90076-2](https://doi.org/10.1016/0012-821X(86)90076-2).
- Stähler, S.C., Panning, M.P., Vance, S.D., Lorenz, R.D., van Driel, M., Nissen-Meyer, T., Kedar, S., 2018. Seismic wave propagation in Icy Ocean worlds. *J. Geophys. Res. Planets* 123 (1), 206–232. <https://doi.org/10.1002/2017JE005338>.
- Tharinema, S., Panning, M.P., Stähler, S.C., Vance, S., Boehm, C., van Driel, M., 2019. Estimating ice shell thickness of icy moons from flexural and Crary waves using 3D seismic simulations. In: *AGU Fall Meeting Abstracts*, 2019, P53D-3479.
- Tsuji, D., Teanby, N.A., 2016. Europa's small impactor flux and seismic detection predictions. *Icarus* 277, 39–55. <https://doi.org/10.1016/j.icarus.2016.04.036>.
- Van Driel, M., Krischer, L., Stähler, S.C., Hosseini, K., Nissen-Meyer, T., 2015. Instaseis: instant global seismograms based on a broadband waveform database. *Solid Earth* 6 (2), 701–717. <https://doi.org/10.5194/se-6-701-2015>.
- Vance, S.D., Kedar, S., Panning, M.P., Stähler, S.C., Bills, B.G., Lorenz, R.D., Huang, H. H., et al., 2018a. Vital Signs: Seismology of Icy Ocean Worlds. *Astrobiology* 18 (1), 37–53. <https://doi.org/10.1089/ast.2016.1612>.
- Vance, S.D., Panning, M.P., Stähler, S., Cammarano, F., Bills, B.G., Tobie, G., Kamata, S., et al., 2018b. Geophysical Investigations of Habitability in Ice-Covered Ocean Worlds. *J. Geophys. Res. Planets* 123 (1), 180–205. <https://doi.org/10.1002/2017JE005341>.